Wavelet-Integrated Alternating Sparse Dictionary Matrix Decomposition in Thermal Imaging CFRP Defect Detection

Junaid Ahmed, Bin Gao, *Senior Member, IEEE*, and Wai Lok Woo, *Senior Member, IEEE*

***Abstract*—With the increasing importance of using carbon fiber reinforced polymer (CFRP) composite in the aircraft industry, it becomes ever more critical to monitor the quality and health of CFRP during the manufacturing process as well as the in-service procedure. The most common types of defects in the CFRP are debonds and delaminations. It is difficult to detect the inner defects on a complex-shaped specimen using conventional nondestructive testing (NDT) methods. In this paper, an unsupervised machine learning method based on wavelet-integrated alternating sparse dictionary matrix decomposition is proposed to extract the weaker and deeper defect information for CFRP by using the optical pulse thermography (OPT) system. We propose to model the low-rank and sparse decomposition jointly in an alternating manner. By incorporating the low-rank information into the sparse matrix and vice versa, the weaker defects will be more efficiently extracted from noise and background. In addition, the integration of wavelet analysis with dictionary factorization enables an efficient time-frequency mining of information and significantly removes the high frequency noise as well as boosts the speed of computations. To investigate the efficacy and robustness of the proposed method, experimental studies have been carried out for inner debond defects on both regular- and irregular-shaped CFRP specimens. A comparative analysis has also been undertaken to study the proposed method against the general OPTNDT methods. The MATLAB demo code can be linked: http://faculty.uestc.edu.cn/gaobin/zh_CN/lwcg/153392/list/index.htm.**

***Index Terms*—Carbon fiber reinforced polymer (CFRP) composites, low-rank decomposition, optical thermography, sparse matrix factorization, wavelet analysis, weak signal detection.**

I. Introduction

In recent years, composite materials have gained wide recognition in the aerospace industry. Manufacturers recommend the use of composites in fuselags and wings of the aircraft pertaining to the useful properties of the composites, such as lightweight, susceptibility to corrosion, and low cost [1]. Due to the unique inhomogeneous structure of the composites, good bonding between the layers is required and usually the defects, such as delaminations and debonds, limit the use of composites [2]. The defects occurring can be attributed to material usage while manufacturing, and environmental and loading effects in service of the composites. Delaminations and debonds are usually at the subsurface of the composite and are thus difficult to be detected by the naked eye. Thus, nondestructive testing (NDT) is the most popular method for detecting defects without any damage to the samples.

In terms of defect detection and characterization, the use of NDT has been emphasized in [3] and [4] to monitor the structural health of the composite. Recently, many researchers have proposed various NDT methods that generally differ in the use of external excitation sources. These methods include, but are not limited to, eddy current [5], [6], ultrasonic [7], acoustic emission [8], and microwave NDT methods [9], [10]. Following the current trends in infrared (IR) technology, many researchers have inclined toward the optical pulse thermographic (OPT) NDT techniques [11]–[15]. A more concise review of the application, usage, and limitations of OPT can be found in [16] and [17]. The prime advantage of using OPT can be drawn as its noncontact nature and fast inspection capability.

In [18], Ryu *et al.* conducted light on the external excitation devices that can be used for the optical thermography NDT. In [19], Chulkov and Vavilov used xenon and halogen lamps as external sources for the OPT. In the process of defect detection using the optical thermography, an external source is used to induce the temperature variations from a fixed distance on a specimen. The temperature variations that represent the time series of the temperature profile are recorded by an IR camera for further processing. Generally, these recorded frames are corrupted with strong noise, and the image resolutions are poor. For successful extraction of the defect information, image inspection techniques are used [20]–[24].

In [25], Winfree *et al.* proposed a technique based on singular value decomposition called the principal component analysis (PCA) for defect detection in composites. In [26], Maldague *et al.* have used pulsed phase thermography (PPT) techniques for defect analysis in the composites. In [27], another efficient defect detection algorithm is proposed based on the polynomial

Manuscript received September 12, 2018; revised November 7, 2018; accepted November 11, 2018. Date of publication November 16, 2018; date of current version July 3, 2019. Paper no. TII-18-2376. *(Corresponding author: Bin Gao.)*

J. Ahmed and B. Gao are with the University of Electronic Science and Technology of China, Chengdu 610054, China (e-mail: junaid_ahmedtl@hotmail.com; bin_gao@uestc.edu.cn).

W. L. Woo is with the School of Electrical and Electronic Engineering, Newcastle University, Newcastle upon Tyne NE1 7RU, U.K. (e-mail: lok.woo@ncl.ac.uk).

Color versions of one or more of the figures in this paper are available online at http://ieeexplore.ieee.org.

Digital Object Identifier 10.1109/TII.2018.2881341

fitting on the logarithmic data called the thermal signal reconstruction (TSR) algorithm. In [28], Katunin proposed a wavelet-domain-based algorithm for defect detection by utilizing both ultrasonic and optical images in the wavelet domain. In [29], Yang *et al.* used the wavelets approach to mine the transient-spatial patterns and proposed an algorithm for defect analysis. In [30], Liang *et al.* proposed the use of wavelet analysis along with the PCA algorithm for low energy impact damage detection in carbon fiber reinforced polymer (CFRP) composites. In [31], Ahmed *et al.* proposed a wavelet-domain-based algorithm utilizing the temporal averaging on the multilevel wavelet decomposition images. In [32], Wu *et al.* proposed sparse principal component thermography for subsurface debond detection in composites. In [33] Peng *et al*. proposed ensemble variational Bayes tensor factorization algorithm (EVBTF) for debond defect analysis in the CFRP specimen. In [34], Ahmed *et al.* proposed a sparse low-rank matrix factorization (S-MoG) algorithm for quantitative defect analysis in the CFRP specimen.

Both EVBTF [33] and S-MoG [34] algorithms obtained good results for flat-shaped CFRP specimen with debonds at small depth levels. However, the algorithms fail to perform for CFRP composites with an irregular shape. In addition, the computational cost of both S-MoG [34] and EVBTF [33] algorithms is quite high as they employ a multilayer factorization architecture. Notwithstanding the above, these algorithms model the multilayer matrix decomposition structure for defect extraction that limits their performance for detecting weaker defects on a complex and irregular surface. To alleviate this problem, we propose a wavelet-integrated alternating sparse dictionary matrix decomposition (WIASDMD). The model allows low-rank and sparse matrix in an alternative optimization approach. The proposed model is able to improve the resolution of the deeper defects present on the irregular surface CFRP composite. In addition, the computational cost and high-frequency noise are minimized by integrating the wavelet processing. To prove the robustness of the algorithm, eight different CFRP specimens with different sizes of the debond defects at various depth levels are used. Both comparative analysis and F-score determination [33] have been undertaken with other OPTNDT algorithms.

The rest of this paper has been organized as follows—The details of the proposed approach are described in Section II. The details of the experimental setup and specimen under test are given in Section III. The result analysis is carried out in Section IV. Finally, conclusions and further work are outlined in Section V.

II. Proposed Defect Extraction Algorithm

A. Optical Pulse Thermography

Owing to the unique properties of the OPT, it is considered a potential NDT and structural health monitoring technology. OPT technology utilizes an external heating source and an IR camera. The specimen is excited using external sources, and temperature variations are captured using the IR camera. The pulse generator is used to control the frequency of excitation and a computer is used to store the results. For the experiments, we have used the surface heating thermography (SHT) [35] mechanism of the OPT. The reflection mode configuration is used with the halogen lamps as the source of heating. The halogen lamps and the IR camera are placed facing the same direction for the reflection mode as can be observed from the schematic diagram of OPT in Fig. 1.

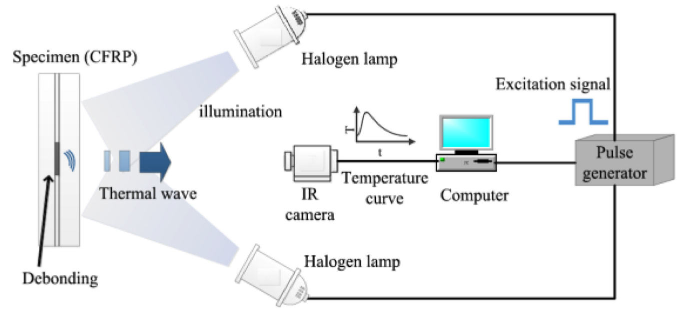

Fig. 1. Schematic diagram of the OPT system.

When the excitation source is applied on the specimen, due to the heating and cooling principle, a temperature change occurs in the specimen. If defects such as delaminations or debonds are present, the fluctuations are observed in the temperature of the specimen. The IR camera captures the time series of these temperature variations and image processing algorithms can be applied to extract the defect information. Considering the OPT with the SHT mechanism [35], the general heat equation is given by the following:

$$\frac{\partial^2 T}{\partial y^2} = \frac{1}{\mu}\frac{dT}{dt} \tag{1}$$

where T is the surface temperature, μ is the thermal diffusivity, and t, y are, respectively, the time and depth of the specimen. Considering the ideal pulse scenario and assuming that the heat flux is applied uniformly on the semi-infinite specimen at a given time instant, the surface temperature can be expressed as

$$T\left(y,t\right) = \frac{E}{e\sqrt{\pi t}} e^{-\frac{y^2}{4\mu t}} \tag{2}$$

where e is the heat effusivity and E is the energy applied on the specimen surface. Considering the heating energy emission from the surface of the specimen, we take $y = 0$ in (2), namely

$$\Delta T\left(t\right) = \frac{E}{e\sqrt{\pi t}} t^{-0.5} \tag{3}$$

where ΔT represents temperature change after external heating is used.

B. Proposed Algorithm

Given a tensor matrix $X \in \mathbb{R}^{m\times n\times k}$ containing the time series of the thermographic sequences, (m, n) is the size of the thermographic image and k is the number of frames. Each frame k in the tensor matrix X is decomposed by the wavelet transform up to two levels by using an undecimated wavelet transform [36], [37] with $\mathrm{sym}29$ wavelet filters. The wavelet transform decomposes the image into an approximation image and three wavelet subband images. As the wavelet subband images (horizontal, vertical, and diagonal) are obtained by the high-pass wavelet

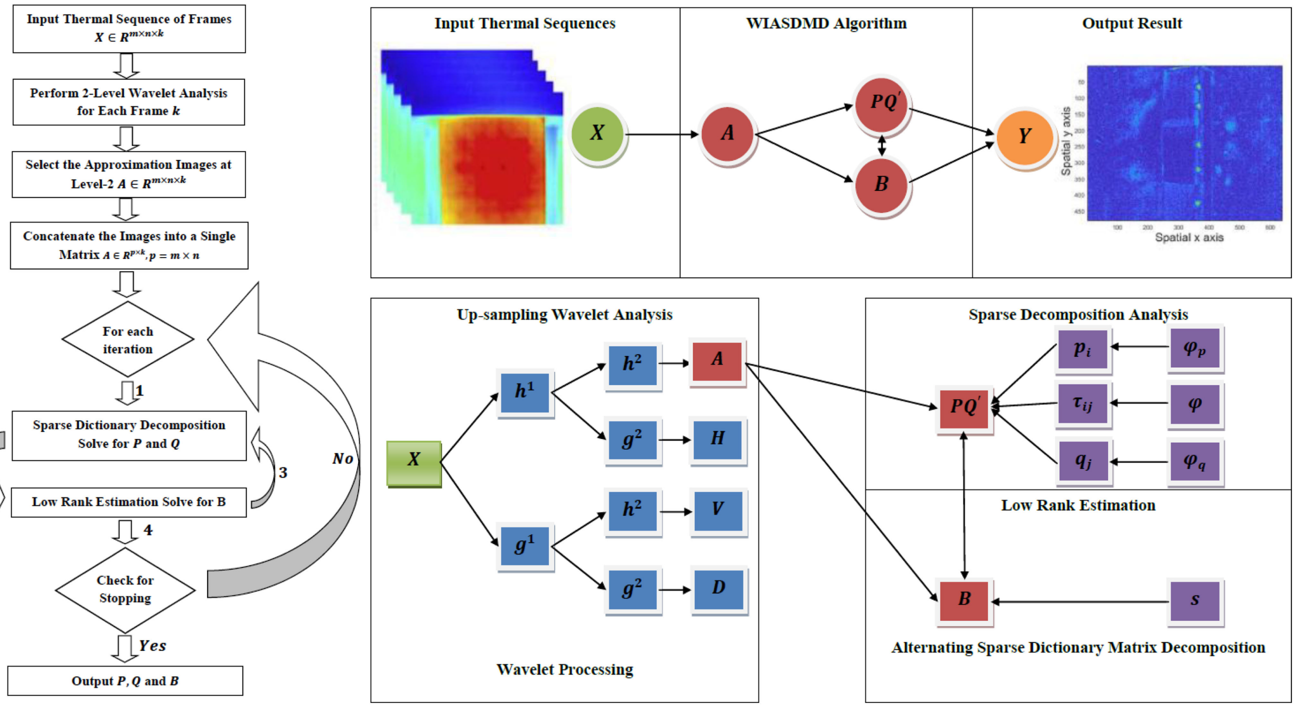

Fig. 2. Main steps of the proposed WIASDMD model.

filters, most of the high-frequency components are extracted from the thermographic images. We take only the approximation images and discard the wavelet subband images as most noise information is contained therein. After the wavelet processing, we perform the proposed alternating sparse low-rank modeling to extract the defect information. The general steps can be seen in Fig. 2.

Given the wavelet domain tensor $A \in \mathbb{R}^{m\times n\times k}$, we can break down the given tensor into the low-rank matrix B, sparse matrix (PQ'), and the noise matrix N_o as

$$A = B + (PQ') + N_o. \tag{4}$$

To extract the weak defect information, we propose the following matrix decomposition problem:

$$\min_{B,P,Q} \left\{ s\,\mathrm{rank}\,(B) + \varphi_p \|P\|_{2,0} + \varphi_q \|Q\|_{2,0} + \|A - B - PQ'\|_F^2 \right\} \tag{5}$$

where$s$ controls the rank of B and φ_p, φ_q are the regularizing parameters for P and Q, respectively, since $PA^{-1}AQ'$ holds for any $m \times n$ nonsingular matrix A.

The problem in (5) is complex and a general regularization framework can be used to represent the problem by imposing the penalties on P and Q. In addition, the convex proxies can be used to relax the rank of matrix B by using the nuclear norm $\|B\|_*$ and $l_{2,2}$ norm in place of $l_{2,0}$ norm. The problem can be reformulated as

$$\min_{B,P,Q} \left\{ s\,\|B\|_* + \frac{\varphi_p}{2}\,\|P\|_2^2 + \frac{\varphi_q}{2}\,\|Q\|_2^2 + \|A - B - PQ'\|_F^2 \right\}. \tag{6}$$

The problem of (6) can be divided into two subproblems and they are solved by alternatingly minimizing over the other for each iteration i. The two subproblems can be formulated as follows:

$$(B)^i = \underset{B}{\mathrm{argmin}} \left\{ \left\| B - \left(A - (PQ')^{i-1} \right) \right\|_F^2 + s\|B\|_* \right\} \tag{7}$$

$$(PQ')^i = \underset{P,Q}{\mathrm{argmin}} \left\{ \|(A - B^i) - PQ'\|_F^2 + \frac{\varphi_p}{2}\,\|P\|_2^2 + \frac{\varphi_q}{2}\,\|Q\|_2^2 \right\}. \tag{8}$$

Equation (7) is a classic convex optimization problem and can be solved using the singular value thresholding algorithm [38]. For (8), we solve it using the Bayesian matrix factorization approach [39]. We follow the principles from the MAP theory and solve the problem in (8). Assuming that the noise satisfies Gaussian distribution and the model parameters correspond to the l_2 loss and l_2 regularizer. The probabilistic model for the two suboptimization problems of (7) and (8) is shown in Fig. 3.

For the sake of simplicity, let the term $(A - B^i) = X$ and consider the following optimization problem:

$$\min_{P,Q} \|X - PQ'\|_1 + \frac{\varphi'_p}{2}\,\|P\|_2^2 + \frac{\varphi'_q}{2}\,\|Q\|_2^2. \tag{9}$$

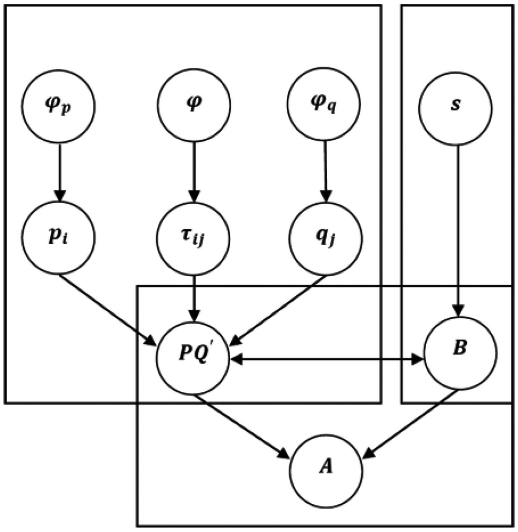

Fig. 3. Probabilistic model for the proposed algorithm.

Solving directly the optimization problem in (9) is computationally expensive as the Laplace distribution is nonsmooth. To solve this problem, we can use a leveled hierarchical form of the Laplacian distribution. Let x be the random variable with the Laplacian distribution its probability differential function can be given as follows:

$$p\left(x\left|p, a^2\right.\right) = \frac{a^2}{2}\exp\left(-a^2\left|x - p\right|\right). \tag{10}$$

The Laplacian distribution has a unique property by which it can be represented as a mixture of Gaussians as

$$L\left(x\left|p, a^2\right.\right) = \int_0^{\infty} \aleph\left(x\left|p, \tau\right.\right)\mathrm{Expon}\left(\tau, a^2\right)d\tau \tag{11}$$

where $\mathrm{Expon}(\tau, a^2)$ represents the exponential distribution. To incorporate this, a matrix $T = [\tau_{ij}] \in \mathbb{R}^{m\times n}$ is used as each element follows an exponential prior for the corresponding x_{ij}. It should be noted that this variable relates the l_1 term to the l_2 term. Thus, a closed-form solution of the problem is possible. Let p_i be the ith row of P and q_j be the jth row of Q. The wavelet-domain-based matrix factorization model can be represented as follows:

$$x_{ij}|P, Q, T \sim \aleph\left(x_{ij}\left|p'_i q_j, \tau_{ij}\right.\right) \tag{12}$$

$$p_{ij}|\varphi_p \sim \aleph\left(p_{ij}\left|0, \varphi_p^{-1}\right.\right) \tag{13}$$

$$q_{ij}|\varphi_q \sim \aleph\left(q_{ij}\left|0, \varphi_q^{-1}\right.\right) \tag{14}$$

$$\tau_{ij}|\varphi \sim \mathrm{Expon}\left(\tau_{ij}|\varphi/2\right). \tag{15}$$

For the problem posted in (12)–(15), the conditional expectation maximization (EM) algorithm is formulated. Let T be the missing data, $\emptyset = [P, Q]$ be the parameters to be estimated, and the parameters φ, φ_p, and φ_q be the fixed hyperparameters. The EM algorithm alternates between two steps, given by the E-step and the M-step. In the E-step, the Q-function is computed, which is also called the log-posterior expectation of the data T. Let the current estimates be $\hat{\emptyset} = [\hat{P}, \hat{Q}]$; then, the Q-function is given as follows:

$$\mathcal{Q}\left(Q\middle|\hat{\emptyset}\right) = E_T\left[\mathrm{logp}\left(Q\middle|\widehat{P}, X, T\right)\middle|X, \hat{\emptyset}\right]. \tag{16}$$

This can be solved by taking log on both sides and ignoring the terms that do not correspond to Q as

$$\begin{aligned}&\mathrm{logp}\left(X\middle|Q, \hat{P}, T\right) + \mathrm{logp}\ (Q)\\ &\quad= -\frac{1}{2}\sum_i^m\sum_j^n\left\{\tau_{ij}^{-1}(x_{ij} - \hat{p}'_i q_j)^2\right\} - \frac{\varphi_q}{2}\sum_j^n q'_j q_j + C.\end{aligned} \tag{17}$$

In (17), the term C is a constant. Now, in order to solve for $E[\tau_{ij}^{-1}|X, \hat{\emptyset}]$ in the E-step, it can be observed that τ_{ij}^{-1} has an inverse gamma distribution. Following this, the posterior expectation can be given by

$$E\left[\tau_{ij}^{-1}\left|X\right., \hat{P}, \hat{Q}\right] = \frac{\sqrt{\varphi}}{|\omega_{ij}|} \triangleq \langle\tau_{ij}^{-1}\rangle \tag{18}$$

where $\omega_{ij} = x_{ij} - (pq')_{ij}$. Next, in the M-step, the parameter Q is updated by maximizing the Q-function in (16). This can be done by computing the partial derivative of the Q-function with respect to q_j and setting it to zero. The update rule can be given by

$$q_j = \left(\hat{P}'\Omega_j\hat{P} + \varphi_q I_\omega\right)^{-1}\hat{P}'\Omega_j x._j \tag{19}$$

where $\Omega_j = \mathrm{diag}(\langle\tau_{1j}^{-1}\rangle, \ldots, \langle\tau_{mj}^{-1}\rangle)$ and $x._j$ is the jth column of X. Following the same convention, the updated formula for p can be found as

$$p_i = \left(\hat{Q}'\Lambda_i\hat{Q} + \varphi_p I_\omega\right)^{-1}\hat{Q}'\Lambda_i x_i. \tag{20}$$

where $\Lambda_i = \mathrm{diag}(\langle\tau_{i1}^{-1}\rangle, \ldots, \langle\tau_{\mathrm{in}}^{-1}\rangle)$ and $x_i.$ is the ith row of X. The stopping condition for this problem is set as

$$\sum_i \frac{(\omega_{ij}^i - \omega_{ij}^{i-1})}{\omega_{ij}^{i-1}} < \mathrm{tol}. \tag{21}$$

The term tol represents the tolerance level that has been selected to be 10^{-2} based on an independent Monte Carlo test. For (7), this is solved by the singular value thresholding (SVT) [38]. Finally, the stopping criteria are set as follows:

$$\frac{\|B^i - B^{i-1}\|_F}{\|A\|_F} \leq \in \text{ or } \frac{\left\|(PQ')^i - (PQ')^{i-1}\right\|_F}{\|A\|_F} \leq \in \tag{22}$$

where $\in = 10^{-4}$. The complete step-by-step description is tabulated in Table I.

III. Experimental Setup and Specimen Information

A. Experiment Setup

The OPT system is shown in Fig. 4. In our experimental analysis, the halogen lamps are used as the excitation source. The CFRP specimen sample is held using a bracket facing opposite the halogen lamps and the IR camera. The IR camera is A655sc.

TABLE I
PROPOSED WIASDMD

1. Input Data $\boldsymbol{X} \in \boldsymbol{R}^{m\times n\times k}$
2. Perform two-level wavelet decomposition using SWT and get $\boldsymbol{A} \in \boldsymbol{R}^{m\times n\times k}$
3. Convert the tensor A into matrix form.
4. Initialize the parameters $\boldsymbol{\varphi_p}, \boldsymbol{\varphi_q}$ as 1 and $\boldsymbol{P}, \boldsymbol{Q}$ randomly.
5. For each iteration $\boldsymbol{i}$ do;
6. Solve for $\boldsymbol{B}$using the Eq. 7.
7. Solve for **P** and **Q** using the EM algorithm.
8. E-Step: for **P** and **Q**: $\langle \boldsymbol{\tau}_{ij}^{-1} \rangle = \frac{\sqrt{\varphi}}{|\omega_{ij}|}$
9. M-Step: For $\boldsymbol{j}^{th}$ row $\boldsymbol{q_j}$ of $\boldsymbol{Q}$;
10. $\boldsymbol{\Omega_j} = \boldsymbol{diag}\left(\langle \boldsymbol{\tau}_{1j}^{-1} \rangle, \cdots, \langle \boldsymbol{\tau}_{mj}^{-1} \rangle\right)$
11. $\boldsymbol{q_j} = \left(\widehat{\boldsymbol{P}}'\boldsymbol{\Omega_j}\widehat{\boldsymbol{P}} + \boldsymbol{\varphi_q}\boldsymbol{I_\omega}\right)^{-1}\widehat{\boldsymbol{P}}'\boldsymbol{\Omega_j}\boldsymbol{x_{\cdot j}}$
12. For $\boldsymbol{i}^{th}$ row $\boldsymbol{p_i}$ of $\boldsymbol{P}$;
13. $\boldsymbol{\Lambda_i} = \boldsymbol{diag}(\langle \boldsymbol{\tau}_{i1}^{-1} \rangle, \cdots, \langle \boldsymbol{\tau}_{in}^{-1} \rangle)$
14. $\boldsymbol{p_i} = (\widehat{\boldsymbol{Q}}'\boldsymbol{\Lambda_i}\widehat{\boldsymbol{Q}} + \boldsymbol{\varphi_p}\boldsymbol{I_\omega})^{-1}\widehat{\boldsymbol{Q}}'\boldsymbol{\Lambda_i}\boldsymbol{x_{i\cdot}}$
15. Check the stopping criteria using the Eq. 21 and Eq. 22
16. End for
17. Output: **B, P, and Q**

The Matlab demo code can be linked:
http://faculty.uestc.edu.cn/gaobin/zh_CN/lwcg/153392/list/index.htm

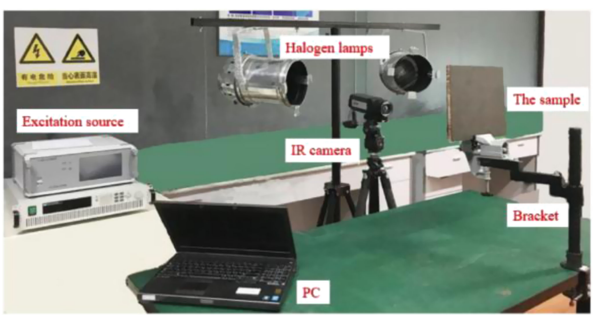

Fig. 4. OPT system at our lab.

It comes with an uncooled vanadium oxide detector. For our experiments, we have used a 50-Hz frame rate to capture the time series of the thermal frames. The IR camera A655sc can detect temperature changes as low as 50 mK.

Eight different CFRP specimens are chosen for the experimental analysis. Among them, three are flat-shaped samples that have subsurface debond defects. The defects have different diameters and depths. The other five specimens are more challenging; they are elbow-shaped CFRP specimen having debond defects at the elbow location. The details about their dimensions and depth information can be found in Table II. The debond defects are made by using the Teflon inserts. Teflon is widely used to simulate the debond defects [2], [40]. It is used owing to its unique properties that are very similar to the actual debond defects. More details can be found in [2] and [40].

IV. Experiments Results and Discussion

A. Wavelet Analysis

Experimental analysis is carried out for the choice of basis function and the number of level decomposition for the wavelet analysis. It should be noted that, in general, there is no hard and fast rule for the choice of basis function in the wavelet analysis. It solely depends on the application and data. In the proposed algorithm, the wavelet decomposition is performed on the entire raw thermal sequence rather than on the selected samples. The main reason behind doing the wavelet decomposition is to remove the high-frequency noise while preserving the low-frequency information. Moreover, by doing the wavelet analysis, we are able to boost the speed of the algorithm as wavelets have an inherent sparse property.

The proposed algorithm was tested with a number of wavelet basis and results are presented in Fig. 5 where specimen 1 is taken as an example. It can be seen from the figure that *symlets* basis gives a good performance in the experimental analysis when compared with other wavelet bases. The choices of the basis function and number of levels were evaluated on the basis of experimental analysis based on the Monte Carlo approach where the process is repeated over ten realizations of using different basis functions and levels in order to obtain the optimal results. With this strategy, the level-2 wavelet decomposition was chosen based on the wavelet-integration results with sparse dictionary decomposition. The proposed algorithm was tested for each specimen using the same mechanism, and symlets basis with level-2 was selected. The task of determining the number of levels is quite crucial. If we increase the number of wavelet levels, the computational cost of the algorithm will increase drastically. The wavelet level comparison results are shown in Fig. 6 for specimen 6.

It can be observed from the figure that increasing the number of levels beyond two levels does not give much improvement; rather, the downside is the increase in a number of levels that results in an increase in the computational cost.

B. Model Analysis

The main reason behind model analysis is to validate the robustness of the algorithm. The proposed model is the integration of the wavelet analysis with the sparse dictionary matrix decomposition. To show the necessity of this integration, we decompose this model into three scenarios. In the first scenario, we evaluate the raw thermal sequences for defect detection using only the wavelet analysis. As in the proposed model, the wavelet analysis is performed on the entire thermal sequence. The result shown is the best frame in the entire thermal sequence. In the second scenario, we perform the sparse dictionary decomposition on the raw thermal frames and show the results. Finally, we compare these results with the proposed model.

Fig. 7 shows the results on the three scenarios for specimen 3. It can be analyzed from the figure that both contrast and resolution of the wavelet decomposition and sparse dictionary are quite poor. By integrating the wavelet analysis and sparse dictionary in an alternating sparse dictionary approach, we are able to improve the resolution of the defects as well as the contrast.

Figs. 8 and 9 show the model comparison results on three scenarios for specimens 5 and 7. Here, the effect on the resolution of the defects is quite evident. The contrast of the defects is significantly improved by the proposed model. It can be concluded that

TABLE II
INFORMATION ABOUT THE CFRP SPECIMEN

Number	Defect Profile	Dimension(mm)	Defect Information(mm) Top Depth, Bottom Diameters	Picture
1	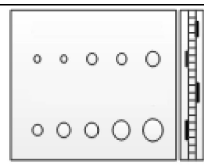	250×250×24.2	2 , 2.2 2,4,6,8,10,12,16,20	
2	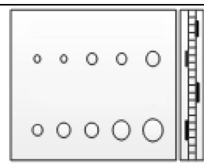	450×300×22	1 , 2 6,10,15	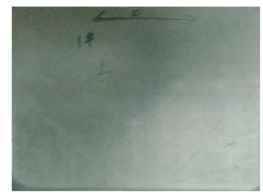
3	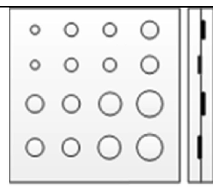	250×250×22.2	2 , 2.2 2,4,6,8	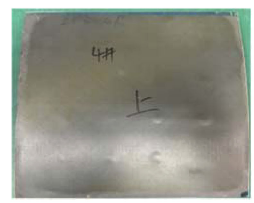
4	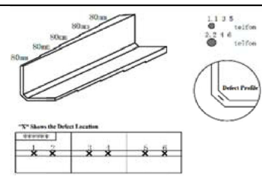	100×100×80	2 , 2.5 3, 6	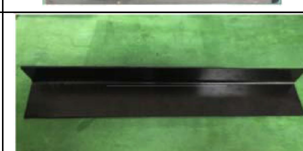
5	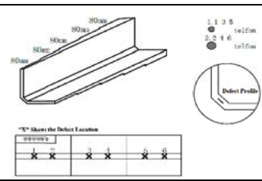	100×100×80	2 , 2.5 6, 8	
6	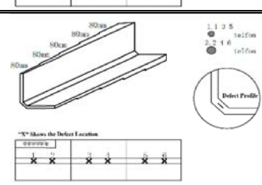	100×100×80	2 , 2.5 9, 10	
7	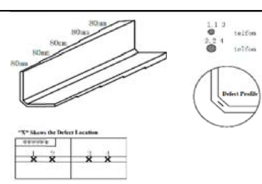	100×100×80	0.5, 0.75, 1, 1.25 3, 6	
8	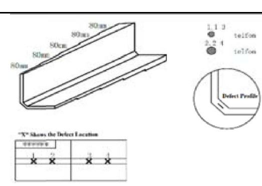	100×100×80	2, 2.25, 2.5, 2.75 3,6	

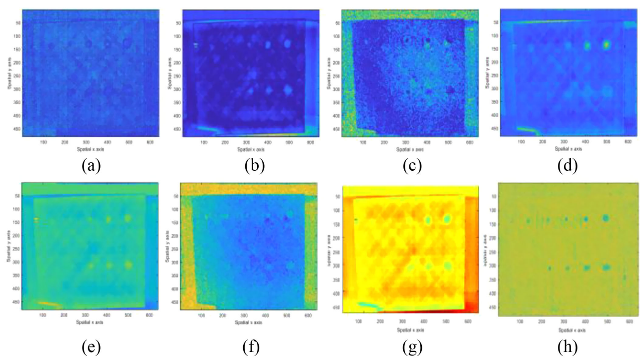

Fig. 5. Wavelet basis analysis for specimen 1. (a) Haar wavelets. (b) Daubechies wavelets. (c) Biorthogonal wavelets. (d) Reverse biorthogonal wavelets. (e) Coiflets. (f) Meyer wavelets. (g) Morlet. (h) Symlets.

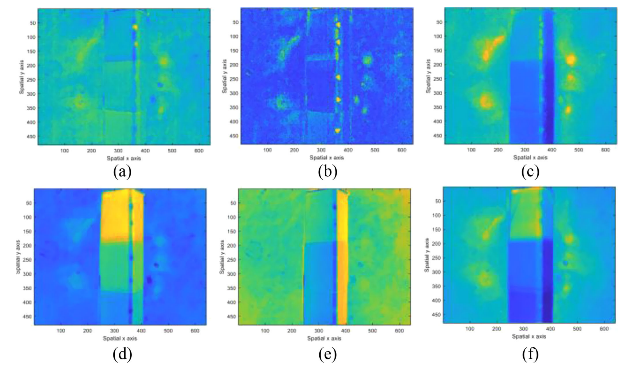

Fig. 6. Wavelet level analysis for specimen 6. (a) Level-1 decomposition. (b) Level-2 decomposition. (c) Level-3 decomposition. (d) Level-4 decomposition. (e) Level-5 decomposition. (f) Level-6 decomposition.

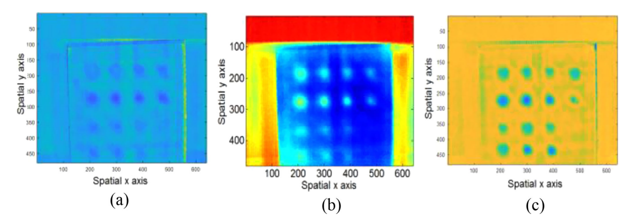

Fig. 7. Model analysis for specimen 3. (a) Wavelet decomposition. x (b) Sparse dictionary decomposition. (c) Proposed model.

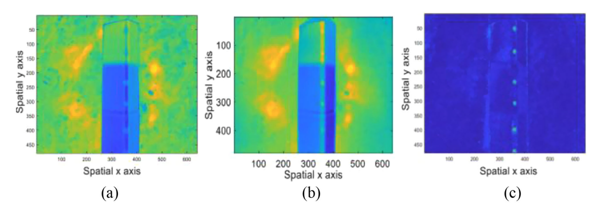

Fig. 8. Model analysis for specimen 5. (a) Wavelet decomposition. (b) Sparse dictionary decomposition. (c) Proposed model.

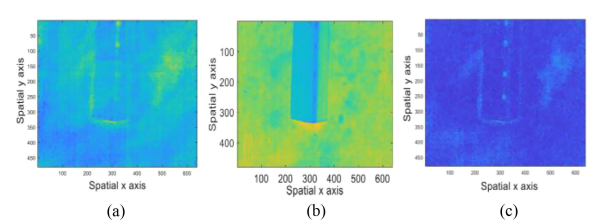

Fig. 9. Model analysis for specimen 7. (a) Wavelet decomposition. (b) Sparse dictionary decomposition. (c) Proposed model.

the proposed WIASDMD is able to mine useful low-rank and sparse information for detecting debond defects using the OPT.

C. Comparison Analysis With General OPTNDT Algorithms

The quantitative detection results are obtained. In order to validate the proposed model and show its robustness, a comparative analysis with general OPTNDT algorithms is presented. The algorithms are compared on the basis of *F*-score and computational time. The algorithms in comparison are PCA [25], PPT [26], TSR [27], EVBTF [33], and S-MoG [34] algorithms. All the algorithms are tested for debond detection in CFRP composites. The comparative results based on *F*-score and consumption time are given in Table III.

The *F*-score is used for quantitative assessment of defect detection. It is based on precision (*P*) and recall (*R*) parameters. The *F*-score is calculated as follows:

$$F = \frac{(P \times R) \times (\alpha + 1)}{(P + R) \times \alpha^2} \tag{23}$$

where α is the relative parameter between P and R. In our experiments, it is equal to 1 implying that the weightage of P is the same as that of R. P and R are evaluated as [33] follows:

$$P = \frac{\mathrm{TP}}{\mathrm{TP} + \mathrm{FP}} \tag{24}$$

$$R = \frac{\mathrm{TP}}{\mathrm{TP} + \mathrm{FN}} \tag{25}$$

where TP is the true positive, it implies that a defect is present and it is detected. FP is the false positive, it implies that a defect is not present but it is detected. FN is the false negative, it implies that a defect is present and it is not detected. The *F*-score is calculated by visually observing the results and perception of the defects. One may argue observing the particular image about the presence or absence of the defect information. In our experimental analysis, the *F*-score is calculated and double validated by human judgment to avoid any discrepancy.

Fig. 10 (row 1) shows the visual results for specimen 1. It is a CFRP sheet with rectangular shape and its defects have depths of 2 or2.2 mm. It has a total of ten defects. It can be seen in Fig. 10 (row 1) that the results of PPT, TSR, PCA, and, EVBTF are somewhat visible, whereas it contains strong noise. If the positions of the defects become unknown, it becomes more difficult to distinguish between the defect regions and the nondefect region. The S-MoG algorithm has a good resolution whereas it can only detect up to six defects. The proposed algorithm has high resolution and it can successfully detect nine out of ten defects. For specimens 2 and 3, the results are shown in Fig. 10 (rows 2 and 3). Specimen 2 has 1 or 2 mm defect depth and the diameter of the defects is quite large (see Table III). Almost all the algorithms perform well, whereas the S-MoG and the

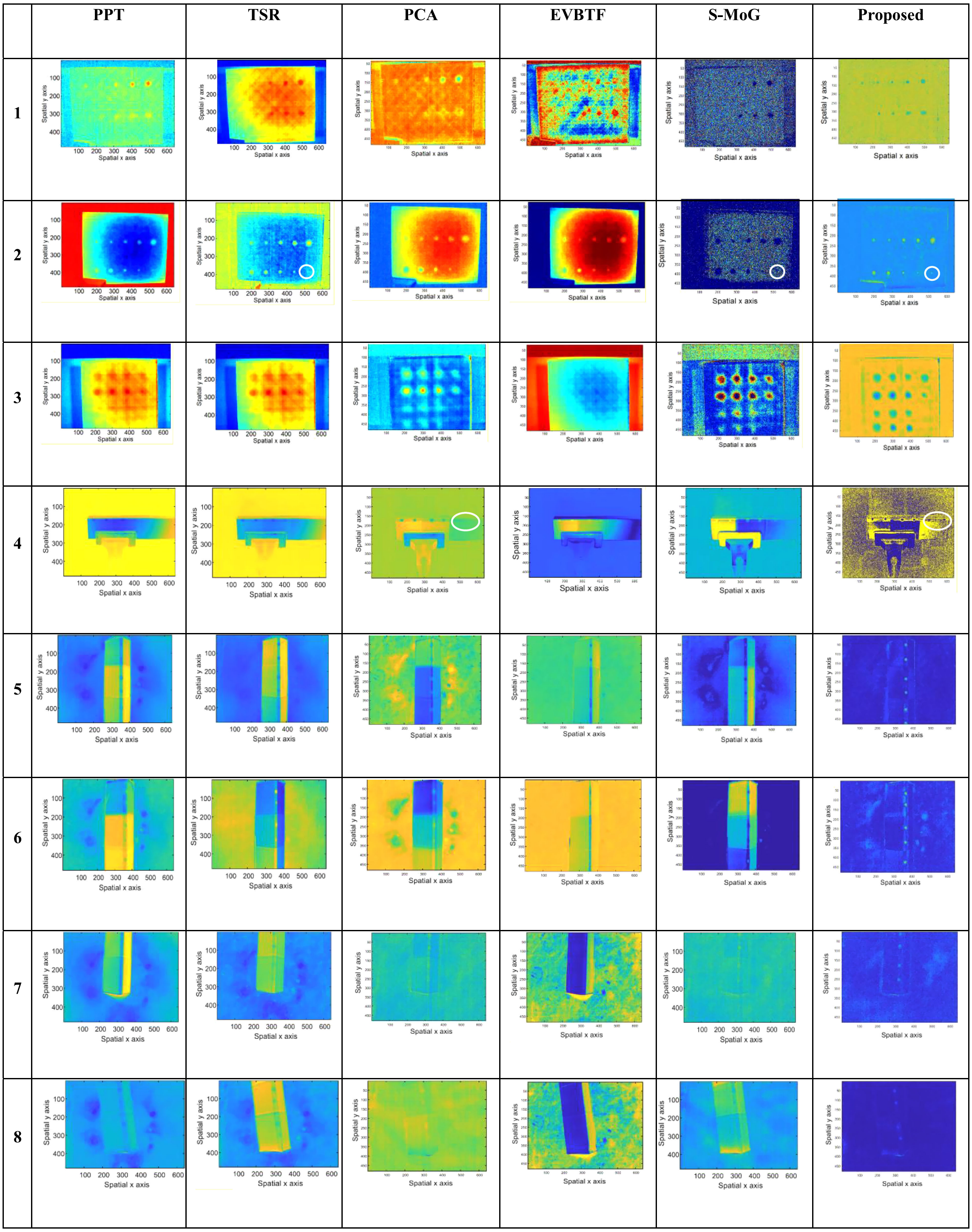

Fig. 10. Visual comparison with general OPTNDT algorithms.

proposed algorithm lead a good resolution that results in better perception of the defects.

Fig. 10 (row 4) shows the comparative results for specimen 4. This is a challenging specimen with irregular R shape. It has defect depths of 2 mm and 2.5 mm with 3 mm and 6 mm diameters. The conventional algorithms fail to perform well and the resolution is quite poor with strong noise. The proposed algorithm is able to detect all the defects clearly. In addition, the shape of the defects is detected clearly with reasonable resolution and noise.

Fig. 10 (rows 5 and 6) shows the comparative results for specimens 5 and 6. These composites have the irregular R shape while the diameters of the defects are quite high (see Table II). The conventional OPTNDT algorithms detect the defects with a

TABLE III
COMPARATIVE RESULTS *F*-SCORE (LEFT) AND TIME TAKEN (RIGHT, IN SECONDS)

Specimen Number	PPT		TSR		PCA		EVBTF		S-MoG		Proposed	
1	0.46	151	0.75	579	0.75	52	0.75	905	0.75	169	**0.94**	**96**
2	0.94	135	0.94	271	0.94	43	0.94	1342	0.94	173	**1**	**103**
3	0.66	564	0.66	642	0.85	153	0.30	1019	0.93	466	**0.93**	**210**
4	0.66	129	0.79	241	0.79	15	0.79	766	0.79	86	**1**	**46**
5	0.79	124	0.79	631	0.79	30	0.49	1039	0.79	120	**1**	**81**
6	0.88	146	0.88	601	0.75	47	0.57	753	0.88	125	**1**	**75**
7	0	132	0.66	568	0.66	43	0	689	0.66	130	**1**	**71**
8	0.66	150	0.86	496	0.66	52	0	789	0.66	140	**1**	**65**
Average	63%	191	79%	504	77%	54	48%	913	80%	176	**98%**	**93**

TABLE IV
COMPARATIVE RESULTS FOR DIFFERENT SIZES OF DEFECTS

Algorithm		Specimen#1 10 Defects	Specimen#2 10 Defects	Specimen#3 16 Defects	Specimen#4 6 Defects	Specimen#5 6 Defects	Specimen#6 5 Defects	Specimen#7 4 Defects	Specimen#8 4 Defects
	(mm)	**Diameters (2,4,6,8,10,12,20)**	**Diameters (6,10,15)**	**Diameters (2,4,6,8)**	**Diameters (3,6)**	**Diameters (6,8)**	**Diameters (9,10)**	**Diameters (6,8)**	**Diameters (3.6)**
PPT	**Detected**	3(10,12,20)	9(10,15)	8(6,8)	3(6)	4(6,8)	4(9,10)	0(0)	2(6)
	Missed	7(2,4,6,8)	1(6)	8(2,4)	3(3)	2(6)	1(9)	4(6,8)	2(3)
TSR	**Detected**	6(6,8,10,12,20)	9(10,15)	8(6,8)	4(6,3)	4(6,8)	4(9,10)	2(8)	3(3,6)
	Missed	4(2,4)	1(6)	8(2,4)	2(3)	2(6)	1(9)	2(6)	1(3)
PCA	**Detected**	6(6,8,10,12,20)	9(10,15)	12(4,6,8)	4(6,3)	4(6,8)	3(9,10)	2(8)	2(6)
	Missed	4(2,4)	1(6)	4(2,4)	2(3)	2(6)	2(9)	2(6)	2(3)
EVBTF	**Detected**	6(6,8,10,12,20)	9(10,15)	4(8)	4(6,3)	2(8)	2(10)	0(0)	0(0)
	Missed	4(2,4)	1(6)	12(2,4,6)	2(3)	4(6,8)	3(9,10)	4(6,8)	4(3,6)
S-MoG	**Detected**	6(6,8,10,12,20)	9(10,15)	14(4,6,8)	4(6,3)	4(6,8)	4(9,10)	2(8)	2(6)
	Missed	4(2,4)	1(6)	2(2)	2(3)	2(6)	1(9)	2(6)	2(3)
Proposed	**Detected**	9(4,6,8,10,12,20)	10(6,10,15)	14(4,6,8)	6(6,3)	6(6,8)	5(9,10)	4(6,8)	4(3,6)
	Missed	1(2)	0(0)	2(2)	0(0)	0(0)	0(0)	0(0)	0(0)

lot of background noise and have poor resolution. However, the proposed algorithm detects all the defects accurately retaining their shape and with reasonable resolution.

Fig. 10 (rows 7 and 8) show the results for specimens 7 and 8. For specimen 6, the defect diameters are 3 and 6 mm. There are a total of four defects having depths of (0.5, 0.75, 1, 1.25) mm. By observing the results for specimen 7, we can see that the proposed algorithm is able to detect deeper defects more clearly in comparison with other algorithms, where the performance depletes drastically. It is almost impossible to observe the presence of defects in some figures. For specimen 8, we have the defect diameters of 3 and 6 mm. Here, we have four defects with depths of (2, 2.25, 2.5, 2.75) mm. From the comparative results, it can be verified that the proposed algorithm can detect debond defects up to depths of 2.75 mm clearly. However, the resolution and contrast of the proposed algorithm is not quite good while the detection is much better in comparison with other general OPTNDT algorithms. It can be argued that using the wavelet domain sparse low-rank factorization and mining the low-rank and sparse data jointly in an iterative manner, one can improve the resolution and performance of the defect detection in the CFRP composites.

Table III shows the *F*-score-based results [33]. We have shown the consumption time of different algorithms. We have averaged the *F*-score values for all the algorithms and quoted them in percentage. On average, the PPT algorithm gives 63% defect detection capability. The TSR, PCA, and EVBTF algorithms give 79%, 77%, and 48% detection capability in terms of F-score, respectively. The algorithm of S-MoG has 80% detection rate. The proposed algorithm gives the highest detection rate on average at 98%. In terms of consumption time, the PCA is the fastest algorithm among all and the slowest one is the EVBTF algorithm. The proposed algorithm gives better execution time. Nonetheless, the proposed algorithm gives the best F-score performance.

Table IV shows the comparative results for different algorithms in detecting defects with different diameters. It can be observed that the general OPTNDT algorithms fail to detect smaller diameter defects on both regular samples as well as on irregular-shaped CFRP specimens. However, the proposed algorithm shows the ability to differentiate the defects more precisely and accurately. The proposed algorithm detects all the defects, whereas only 3 defects were missed from a total of 51 defects on 8 different CFRP samples.

V. Conclusion

This paper proposes a WIASDMD method. The proposed method is tested for detecting inner debond defects using optical thermography. The mining of the sparse and low-rank information jointly in an iterative manner benefits the quantification of the defects from noise and background. The use of wavelet analysis significantly boosted the computational speed of the algorithm and reduced the noise. In the experimental analysis, more challenging CFPR specimens with irregular shape have been validated. The proposed algorithm has shown a high level of performance in defect extraction in terms of F-score. Both quantitative and qualitative results have validated that with relatively low computational cost, the proposed method has successfully modeled the complex noise and extracted the weaker debond defect information. Future research will focus on adapting and testing the proposed method on more composite specimens and testing it with different IR thermography techniques.

References

[1] H. Fernandes, H. Zhang, A. Figueiredo, C. Ibarra-Castanedo, G. Guimarares, and X. Maldague, "Carbon fiber composite inspection and defect characterization using active infrared thermography: Numerical simulations and experimental results," *Appl. Opt.*, vol. 55, no. 34, pp. D46–D53, 2016.

[2] C. Maierhofer, P. Myrach, M. Reischel, H. Steinfurth, M. Röllig, and M. Kunert, "Characterizing damage in CFRP structures using flash thermography in reflection and transmission configurations," *Composites Part B, Eng.*, vol. 57, pp. 35–46, 2014.

[3] A. Poudel, K. R. Mitchell, T. P. Chu, S. Neidigk, and C. Jacques, "Non-destructive evaluation of composite repairs by using infrared thermography," *J. Composite Mater.*, vol. 50, no. 3, pp. 351–363, 2016.

[4] C. Meola, S. Boccardi, G. M. Carlomagno, N. D. Boffa, E. Monaco, and F. Ricci, "Nondestructive evaluation of carbon fibre reinforced composites with infrared thermography and ultrasonics," *Composite Struct.*, vol. 134, pp. 845–853, 2015.

[5] B. Gao, L. Bai, W. L. Woo, G. Y. Tian, and Y. Cheng, "Automatic defect identification of eddy current pulsed thermography using single channel blind source separation," *IEEE Trans. Instrum. Meas.*, vol. 63, no. 4, pp. 913–922, Apr. 2014.

[6] B. Gao, W. L. Woo, Y. He, and G. Y. Tian, "Unsupervised sparse pattern diagnostic of defects with inductive thermography imaging system," *IEEE Trans. Ind. Inform.*, vol. 12, no. 1, pp. 371–383, Feb. 2016.

[7] D. Palumbo, R. Tamborrino, U. Galietti, P. Aversa, A. Tatì, and V. A. M. Luprano, "Ultrasonic analysis and lock-in thermography for debonding evaluation of composite adhesive joints," *NDT E Int.*, vol. 78, pp. 1–9, 2016.

[8] V. Munoz *et al.*, "Damage detection in CFRP by coupling acoustic emission and infrared thermography," *Composites Part B, Eng.*, vol. 85, pp. 68–75, 2016.

[9] A. Foudazi, C. A. Edwards, M. T. Ghasr, and K. M. Donnell, "Active microwave thermography for defect detection of CFRP-strengthened cement-based materials," *IEEE Trans. Instrum. Meas.*, vol. 65, no. 11, pp. 2612–2620, Nov. 2016.

[10] B. Gao, W. L. Woo, G. Y. Tian, and H. Zhang, "Unsupervised diagnostic and monitoring of defects using waveguide imaging with adaptive sparse representation," *IEEE Trans. Ind. Inform.*, vol. 12, no. 1, pp. 405–416, Feb. 2016.

[11] S. Ekanayake, S. Gurram, and R. H. Schmitt, "Depth determination of defects in CFRP-structures using lock-in thermography," *Composites Part B, Eng.*, vol. 147, no. April, pp. 128–134, 2018.

[12] Z. Wang, G. Tian, M. Meo, and F. Ciampa, "Image processing based quantitative damage evaluation in composites with long pulse thermography," *NDT E Int.*, vol. 99, no. April, pp. 93–104, 2018.

[13] H. Zhang *et al.*, "An infrared-induced terahertz imaging modality for foreign insert detection in a glass fiber-skinned lightweight honeycomb composite panel," *IEEE Trans. Ind. Inform.*, 2018, doi: 10.1109/TII.2018.2832244.

[14] L. Zhang, Q. Zhang, B. Du, X. Huang, Y. Y. Tang, and D. Tao, "Simultaneous spectral-spatial feature selection and extraction for hyperspectral images," *IEEE Trans. Cybern.*, vol. 48, no. 1, pp. 16–28, Jan. 2018.

[15] H. Zhang *et al.*, "Optical and mechanical excitation thermography for impact response in basalt-carbon hybrid fiber-reinforced composite laminates," *IEEE Trans. Ind. Inform.*, vol. 14, no. 2, pp. 514–522, Feb. 2018.

[16] V. P. Vavilov, "Modeling and characterizing impact damage in carbon fiber composites by thermal/infrared non-destructive testing," *Composites Part B, Eng.*, vol. 61, pp. 1–10, 2014.

[17] R. Yang and Y. He, "Optically and non-optically excited thermography for composites: A review," *Infrared Phys. Technol.*, vol. 75, pp. 26–50, 2016.

[18] C. H. Ryu, S. H. Park, D. H. Kim, K. Y. Jhang, and H. S. Kim, "Nondestructive evaluation of hidden multi-delamination in a glass-fiber-reinforced plastic composite using terahertz spectroscopy," *Composite Struct.*, vol. 156, pp. 338–347, 2016.

[19] A. O. Chulkov and V. P. Vavilov, "Hardware and software for thermal nondestructive testing of metallic and composite materials," *J. Phys. Conf. Ser.*, vol. 671, no. 1, 2016, Art. no. 012011.

[20] X. Bai, Y. Fang, W. Lin, L. Wang, and B. F. Ju, "Saliency-based defect detection in industrial images by using phase spectrum," *IEEE Trans. Ind. Inform.*, vol. 10, no. 4, pp. 2135–2145, Nov. 2014.

[21] G. Acciani, G. Brunetti, and G. Fornarelli, "Application of neural networks in optical inspection and classification of solder joints in surface mount technology," *IEEE Trans. Ind. Inform.*, vol. 2, no. 3, pp. 200–209, Aug. 2006.

[22] D. M. Tsai, I. Y. Chiang, and Y. H. Tsai, "A shift-tolerant dissimilarity measure for surface defect detection," *IEEE Trans. Ind. Inform.*, vol. 8, no. 1, pp. 128–137, Feb. 2012.

[23] W. C. Li and D. M. Tsai, "Defect inspection in low-contrast LCD images using Hough transform-based nonstationary line detection," *IEEE Trans. Ind. Inform.*, vol. 7, no. 1, pp. 136–147, Feb. 2011.

[24] A. Picon, O. Ghita, P. F. Whelan, and P. M. Iriondo, "Fuzzy spectral and spatial feature integration for classification of nonferrous materials in hyperspectral data," *IEEE Trans. Ind. Inform.*, vol. 5, no. 4, pp. 483–494, Nov. 2009.

[25] W. P. Winfree, K. E. Cramer, J. N. Zalameda, P. A. Howell, and E. R. Burke, "Principal component analysis of thermographic data," *Proc. SPIE*, vol. 9485, 2015, Paper 94850S.

[26] F. López, V. P. Nicolau, and X. Maldague, "Pulsed phase thermography applied on complex structures: Modelling and numerical analysis," in *Proc. 11th Int. Conf. Quant. Infrared Thermography*, 2012, Paper no. 260.

[27] S. M. Shepard and M. F. Beemer, "Advances in thermographic signal reconstruction," *Proc. SPIE*, vol. 9485, 2015, Paper 94850R.

[28] A. Katunin, "Characterisation of impact damage of composite structures using wavelet-based fusion of ultrasonic and optical images," *Adv. Composite Lett.*, vol. 23, no. 5, pp. 123–130, 2015.

[29] H. Yang, B. Gao, G. Tian, W. Ren, and W. L. Woo, "Transient-spatial pattern mining of eddy current pulsed thermography using wavelet transform," *Chin. J. Mech. Eng.*, vol. 27, pp. 768–778, 2014.
[30] T. Liang, W. Ren, G. Y. Tian, M. Elradi, and Y. Gao, "Low energy impact damage detection in CFRP using eddy current pulsed thermography," *Composite Struct.*, vol. 143, pp. 352–361, 2016.
[31] M. Z. Ahmad *et al.*, "Wavelet subspace decomposition of thermal infrared images for defect detection in artworks," *Infrared Phys. Technol.*, vol. 77, pp. 325–334, 2016.
[32] J. Y. Wu, S. Sfarra, and Y. Yao, "Sparse principal component thermography for subsurface defect detection in composite products," *IEEE Trans. Ind. Inform.*, 2018, doi: 10.1109/TII.2018.2817520.
[33] P. Lu, B. Gao, Q. Feng, Y. Yang, W. L. Woo, and G. Y. Tian, "Ensemble variational Bayes tensor factorization for super resolution of CFRP debond detection," *Infrared Phys. Technol.*, vol. 85, pp. 335–346, 2017.
[34] J. Ahmed, B. Gao, G. Y. Tian, Y. Yang, and Y. C. Fan, "Sparse ensemble matrix factorization for debond detection in CFRP composites using optical thermography," *Infrared Phys. Technol.*, vol. 92, pp. 392–401, 2018.
[35] Y. He, R. Yang, H. Zhang, D. Zhou, and G. Wang, "Volume or inside heating thermography using electromagnetic excitation for advanced composite materials," *Int. J. Therm. Sci.*, vol. 111, pp. 41–49, 2017.
[36] E. Matsuyama *et al.*, "A modified undecimated discrete wavelet transform based approach to mammographic image denoising," *J. Digit. Imag.*, vol. 26, no. 4, pp. 748–758, 2013.
[37] Y. Chen and Z. Cao, "Change detection of multispectral remote-sensing images using stationary wavelet transforms and integrated active contours," *Int. J. Remote Sens.*, vol. 34, no. 24, pp. 8817–8837, 2013.
[38] J.-F. Cai, E. J. Candès, and Z. Shen, "A singular value thresholding algorithm for matrix completion," *SIAM J. Optim.*, vol. 20, no. 4, pp. 1956–1982, 2010.
[39] N. Wang, T. Yao, J. Wang, and D.-Y. Yeung, "A probabilistic approach to robust matrix factorization," *Proc. 12th Eur. Conf. Comput. Vis.*, vol. 7578, 2012, pp. 126–139.
[40] P. Theodorakeas, N. P. Avdelidis, C. Ibarra-Castanedo, M. Koui, and X. Maldague, "Pulsed thermographic inspection of CFRP structures: Experimental results and image analysis tools," *Proc. SPIE*, vol. 9062, 2014, no. March, Paper 90620F.

Junaid Ahmed received the B.E. degree in telecommunications engineering from the Mehran University of Engineering and Technology, Jamshoro, Pakistan, in 2010, and the M.S. degree in electrical and electronics engineering from Eastern Mediterranean University, North Cyprus, Turkey, in 2015. He is currently working toward the Ph.D. degree in nondestructive testing and structural health monitoring using infrared thermography at the University of Electronic Science and Technology of China, Chengdu, China.

His current research interests include wavelet processing, debond damage, quantitative nondestructive testing and evaluation, sparse representations, and low-rank matrix factorization.

Bin Gao (M'12-SM'14) received the B.Sc. degree in communications and signal processing from Southwest Jiao Tong University, Chengdu, China, in 2005, and the M.Sc. degree in communications and signal processing with distinction and the Ph.D. degree in statistic signal processing from Newcastle University, Newcastle upon Tyne, U.K., in 2007 and 2011, respectively.

From 2011 to 2013, he was a Research Associate with the Newcastle University, working on wearable acoustic sensor technology. He is currently a Professor with the School of Automation Engineering, University of Electronic Science and Technology of China, Chengdu, China. He has coordinated several research projects from the National Natural Science Foundation of China. He has authored or coauthored more than 60 papers in various journals and international conference proceedings in his areas of interest. His research interests include sensor signal processing, machine learning, social signal processing, and nondestructive testing and evaluation.

Wai Lok Woo (M'09–SM'11) was born in Malaysia. He received the B.Eng. degree (first class Hons.) in electrical and electronics engineering and the Ph.D. degree in signal processing from the Newcastle University, Newcastle upon Tyne, U.K., in 1993 and 1998, respectively.

He is currently the Director of Research of the Newcastle Research and Innovation Institute, as well as the Director of Operations. He is a Reader with Intelligent Signal Processing, Newcastle University. He has authored or coauthored 300 papers on the topics of his research in various journals and international conference proceedings. His major research is in the fields of mathematical theory and algorithms for data science and analytics, including areas of machine learning, data mining, blind source separation, multidimensional signal processing, and signal/image deconvolution and restoration.

Dr. Woo was the recipient of the IEE Prize and the British Commonwealth Scholarship.